Lasers in Manufacturing Conference 2025

Elucidation of the Spatter Suppression Mechanism in Keyhole Welding of Steel Using a 16kW Disk Laser

Yuji SATO, Masahiro TSUKAMOTO[1]

[a]*Joining and Welding Research Institute, Osaka University, Japan*

Abstract

Laser beam welding is widely utilized across various industries, including the automotive, nuclear power plant, and petrochemical sectors, due to its excellent compatibility with remote control and automation. It enables high-quality welding with a smaller heat-affected zone compared to other welding techniques. However, during high-power laser irradiation, spatter generation commonly occurs, which contributes to defects such as weld wall thinning and porosity. In our previous study, we determined that spatter generation is caused by fluctuations in the keyhole during laser irradiation in vacuum conditions. To address this issue, this study employed a multi-spot laser approach in laser beam keyhole welding to develop a spatter-free process, clarifying the effects of multi-spot lasers on spatter suppression..

Keywords: Type your keywords here, separated by semicolons ;

1. Introduction

Austenitic stainless steel type 304 (SS304) is widely utilized in industrial applications due to its excellent corrosion resistance, high-temperature strength, and good workability. Various welding techniques, including arc welding, resistance welding, electron beam welding, and laser welding, are employed for joining SS304. Among these, laser welding has been increasingly adopted in industries such as automotive manufacturing [1] and railway vehicle production [2], owing to its superior automation compatibility, remote operability, and its ability to achieve high-quality welds with a narrow heat-affected zone.

In laser welding, when a high-power density laser beam irradiates the metallic surface, the energy is absorbed at the surface, leading to localized heating and the formation of a molten pool. At sufficient power densities, recoil pressure induced by vaporization results in the formation of a keyhole, which facilitates deep penetration. However, the dynamic behavior of the keyhole and the molten pool often leads to the ejection of molten metal droplets, referred to as spatter. Spatter generation not only degrades weld quality by introducing defects such as porosity and wall thinning, but also impairs process stability. Therefore, elucidating the fundamental mechanisms governing spatter formation and establishing effective suppression strategies are of critical importance. Several approaches have been reported for reducing spatter in laser welding. For example, Kawahito et al. demonstrated that tilting the laser beam 20° forward in the welding direction, under conditions of 6 kW laser power and 150 mm/s travel speed, reduced the number of spatters with diameters over 100 µm to one-third compared to normal incidence [3]. Furthermore, spatter reduction through ambient pressure control has been widely investigated [4–8]. Matsunawa and Katayama et al. reported that bead-on-plate welding under reduced pressure using CO_2 and Nd:YAG lasers yielded high-quality welds with fewer voids in SS304 and aluminum alloy A5058 [4]. Similarly, Naito et al. demonstrated a 65% reduction in spatter mass under reduced pressure (10 kPa) as compared to atmospheric pressure, during high-speed welding of SM490A steel using an 8.3 kW fiber laser [5].

* Corresponding author. Tel.: +0-000-000-0000 ; fax: +0-000-000-0000 .
E-mail address: author@institute.xxx .

In our previous study, we developed a quantitative spatter evaluation technique based on shadowgraph imaging, which revealed that spatter generation under a vacuum pressure of 10 Pa was reduced to 1/60th of that under atmospheric pressure [9]. Additionally, Meng et al. used a glass observation technique to visualize the molten pool in cross-section and associated a suppression in molten pool fluctuation with reduced spatter emission [10]. While these findings collectively demonstrate the effectiveness of reduced pressure in mitigating spatter, the underlying physical mechanisms remain insufficiently understood.In the present study, the primary objective is to elucidate the spatter suppression mechanism in keyhole laser welding. To achieve this, a real-time, in-situ temperature measurement technique was established by integrating the glass transmission method [11 – 13] with two-color pyrometry. This system enables the evaluation of temperature distributions and dynamic behavior within the longitudinal cross-section of the molten pool. Simultaneously, X-ray transmission imaging was employed to visualize the keyhole structure and its temporal evolution during welding. By analyzing the correlation between molten pool thermodynamics, keyhole fluctuations, and spatter formation under varying ambient pressures, this study seeks to clarify the physical origins of spatter suppression in keyhole-mode laser welding.

2. EXPERIMENTAL PROCEDURE

2.1 Laser Welding

Austenitic stainless-steel type 304 (SS304) specimens with dimensions of 50 mm (width) × 50 mm (length) × 3 mm (thickness) were used. Each specimen was securely fixed in place using a jig inside a sealed chamber. The chamber was mounted on a uni-axial translation stage installed at its base, allowing simultaneous movement of the sample and chamber during welding. The upper surface of the chamber was equipped with a quartz glass window featuring anti-reflection coatings on both sides, optimized for infrared wavelengths, to permit laser transmission and facilitate optical access for observation. The internal pressure of the chamber was reduced using a rotary vacuum pump, and high-purity argon gas was introduced to maintain an inert environment. Bead-on-plate welding experiments were conducted at various target pressures under these controlled atmospheric conditions. A continuous-wave (CW) ytterbium-doped disk laser with a central wavelength of 1030 nm and a maximum output power of 16 kW was employed as the heat source. The laser beam was transmitted to the processing head through an optical fiber with a core diameter of 200 µm. The beam exiting the fiber was first collimated and then focused onto the specimen surface using a focusing lens, resulting in a spot diameter of 350 µm at $1/e^2$ intensity. The welding parameters used in the bead-on-plate experiments are summarized in Table 1. The laser power was fixed at 10 kW, and the welding speed was set to 8 m/min. Following laser irradiation, the chamber was purged with argon gas and returned to atmospheric pressure before the specimen was removed for subsequent analysis.

2.2 Imaging Techniques due to capture laser welding dynamics

To elucidate the spatter suppression mechanism during keyhole-mode laser welding, two complementary imaging techniques were employed: X-ray transmission imaging and direct thermal imaging of the molten pool longitudinal section. Figure 1 shows a schematic of the X-ray transmission imaging system utilized to observe keyhole behavior in real time during laser irradiation. X-rays generated by an X-ray source (ISOVOLT 225 HP, Baker Hughes) pass through an optical aperture and irradiate the specimen. Due to variations in X-ray transmittance depending on local material density, internal features such as the keyhole can be visualized. The transmitted intensity distribution is captured by a high-speed video camera (MEMRECAM GX-8, NAC Image Technology) via an image intensifier (E5883RE-P1K, Canon Electron Tube Device) with a residual light time of 0.1 ms. This configuration enabled real-time observation of the dynamic evolution of the keyhole during laser welding. The conditions for X-ray phase contrast imaging are summarized in Table 2. The X-ray source was operated at 110 kV and 7.0 mA, and imaging was conducted at a magnification of 2.7× to enhance spatial resolution.

Figure 2 illustrates the setup for the direct thermal imaging of the longitudinal section of the molten pool during laser irradiation. A borosilicate glass plate (2 mm thick) was closely appressed to the SS304 sample (3 mm thick), allowing visualization of the molten pool profile at the interface. A laser beam was irradiated onto the interface, and the spontaneous thermal emission generated during welding was simultaneously captured at two discrete wavelengths using a two-color lens unit attached to a high-speed video camera.

The temperature distribution was computed using the two-color pyrometry method [14], based on the difference in radiance at two wavelengths. The radiance I′ (λ ,T)I′ (λ ,T) for a given wavelength λ λ and temperature TT can be expressed by Planck's law as:

$$I'(\lambda, T) = \varepsilon_{\lambda \mathrm{T}} \frac{2C_1}{\lambda^5} \exp\left(\frac{-C_2}{\lambda T}\right) \quad (1)$$

Assuming the spectral emissivity ratio $\varepsilon_{\lambda 1T}/\varepsilon_{\lambda 2T} \approx 1 \varepsilon_{\lambda 1T}/\varepsilon_{\lambda 2T} \approx 1$, the true temperature TT can be derived from the luminance temperatures $T_{a1} T_{a1}$ and $T_{a2} T_{a2}$ corresponding to wavelengths λ_1 and λ_2, respectively, using the following equation:

$$T = \left(\left(\frac{1}{\lambda_2 T_{a2}} - \frac{1}{\lambda_1 T_{a1}} - \frac{1}{C_2} ln \left(\frac{\varepsilon_{\lambda_1 T}}{\varepsilon_{\lambda_2 T}} \right) \right) \left(\frac{1}{\lambda_2} - \frac{1}{\lambda_1} \right)^{-1} \right)^{-1} \quad (2)$$

In the present experiment, thermal radiation was simultaneously captured at λ_1=800±20 nm and λ_2=725±20 nm. Calibration was performed using a standard light source under identical camera settings, and temperature calculations were carried out using the Thermias software provided by NAC Image Technology. The processed data enabled real-time, spatially resolved temperature mapping of the molten pool's longitudinal cross-section.

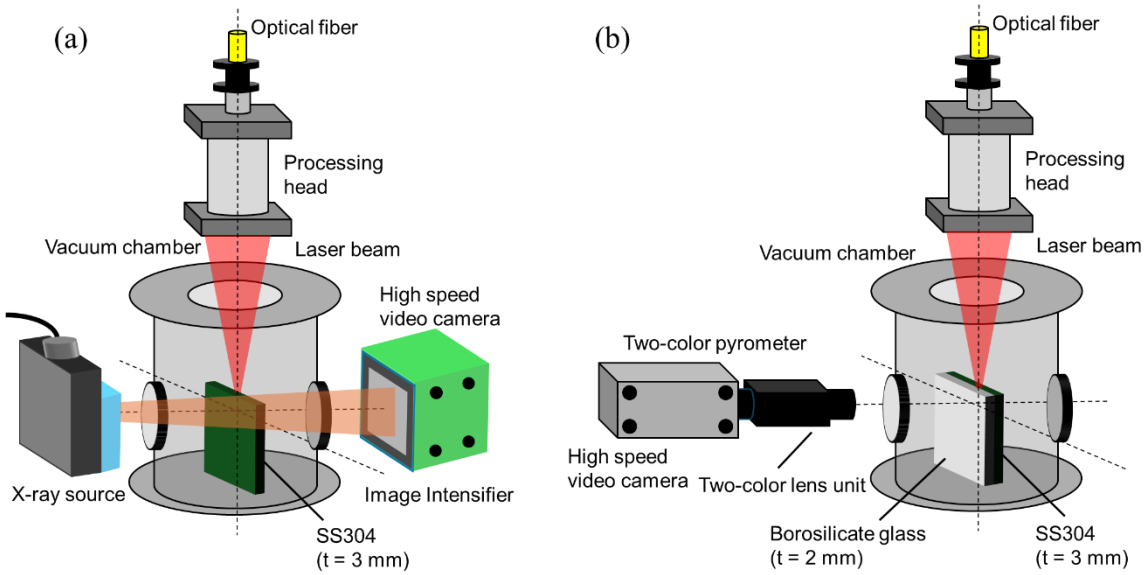

Fig. 1 Experimental set up for laser welding observed using (a) X ray imaging system and (b) 2 color temperature measurement system.

3. Results and Discussion

Figure 2 shows cross-sectional images of the weld beads obtained through macroscopic observation. Central cracking was observed in all specimens, regardless of ambient pressure, though the crack size decreased progressively with reduced pressure. At ambient pressures of 10^3 Pa and above, the fusion zone exhibited a characteristic "wine cup" shape, with the upper portion being noticeably wider than the lower part. In contrast, at 10^2 Pa and below, the fusion zone maintained a nearly uniform width throughout its depth. The bead width increased with rising ambient pressure from 10 Pa to 10^4 Pa, reaching a maximum at 10^4 Pa. Conversely, the penetration depth increased as ambient pressure decreased from 10^5 Pa to 10^2 Pa, with the deepest penetration observed at 10^2 Pa. At 10 Pa, the penetration depth fell between the values obtained at 10^2 Pa and 10^3 Pa.

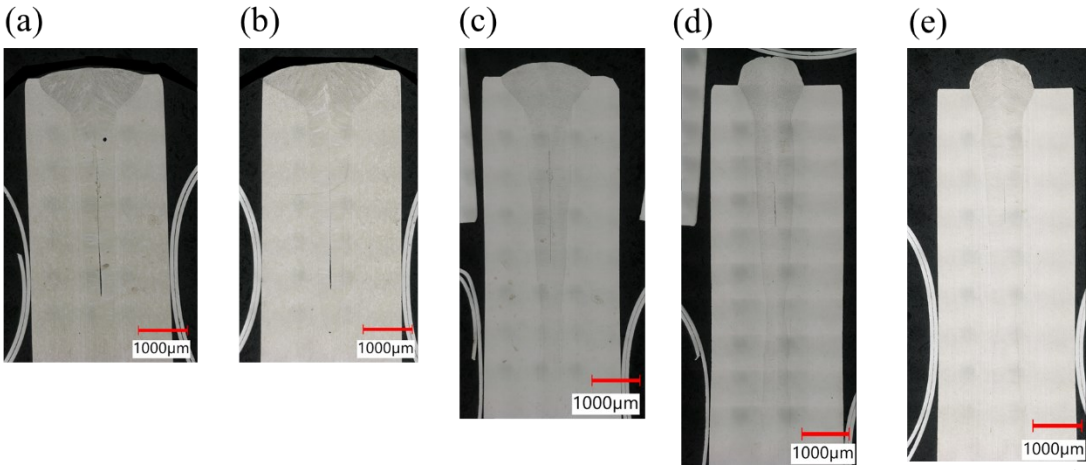

Fig.2 Cross sectional image of laser welding beads obtained under ambient pressure of (a) 10^5, (b) 10^4, (c) 10^3, (d) 10^2, (e)10 Pa, respectively.

Figure 3 presents X-ray transmission images obtained by compositing 50 frames captured during the laser irradiation period between 200 ms and 250 ms. Figures 3(a) to 3(e) correspond to ambient pressures ranging from 10^5 Pa to 10 Pa, respectively. Under ambient pressures of 10^3 Pa and above, the keyhole capillary exhibited a wedge-shaped profile, narrowing toward the bottom. In contrast, at 10^2 Pa and below, the keyhole capillary maintained an almost constant width throughout its depth. The keyhole depth increased progressively as the ambient pressure decreased from 10^5 Pa to 10^2 Pa, reaching a maximum at 10^2 Pa. Similarly, the keyhole opening width expanded with decreasing pressure from 10^4 Pa to 10^2 Pa. The overall keyhole area exhibited an increasing trend with pressure reduction, also peaking at 10^2 Pa. A comparison between the conditions of 10^5 Pa and 10 Pa revealed that the keyhole depth at 10 Pa was approximately 1.5 times greater, the opening width was 1.3 times wider, and the keyhole area was 2.9 times larger than those observed at 10^5 Pa.

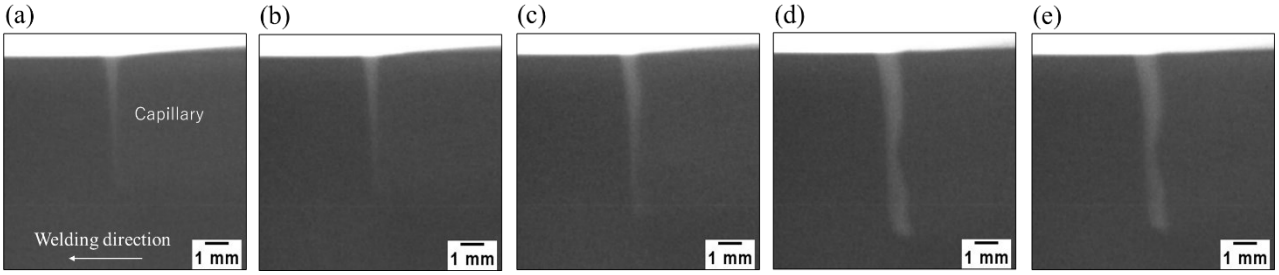

Fig.3X ray image of laser welding beads obtained under ambient pressure of (a) 10^5, (b) 10^4, (c) 10^3, (d) 10^2, (e)10 Pa, respectively.

Figure 4 shows the longitudinal cross-sectional temperature distribution of the molten pool obtained using the two-color pyrometry method. Based on this temperature distribution, regions exceeding the melting point of iron (1500 °C) were defined as the molten pool, and the molten pool area was calculated for each ambient pressure condition. The results revealed a significant difference in molten pool area between conditions at or below 10^2 Pa and those at or above 10^3 Pa. Specifically, under the 10^2 Pa condition, the average molten pool area was 19.2 mm², which was approximately 1.8 times larger than that observed at 10^5 Pa, where the average area was 10.5 mm².

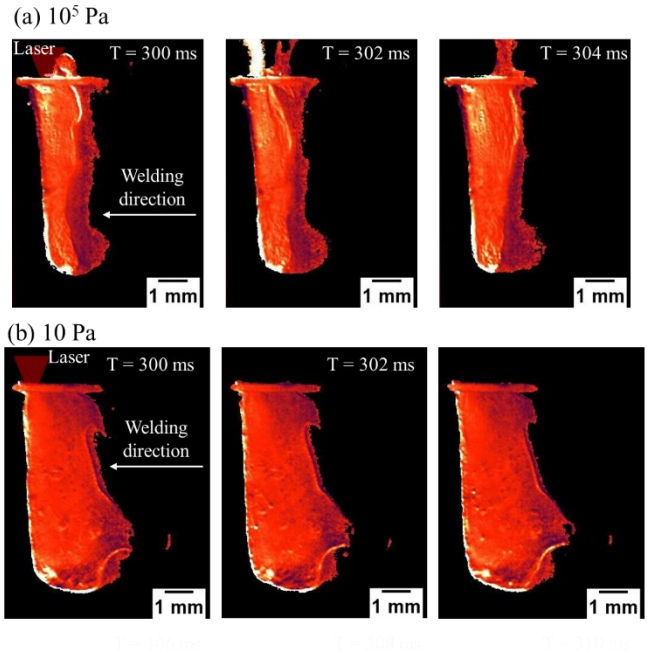

Fig.4 2-color temperature image of laser welding beads obtained under ambient pressure of (a) 10^5, (b) 10^4, (c) 10^3, (d) 10^2, (e)10 Pa, respectively.

Under atmospheric pressure, dense plumes are periodically generated during laser irradiation. These plumes intermittently attenuate the incident laser beam, resulting in periodic reductions in the energy delivered to the material. This leads to repeated contraction of the molten pool. The contraction, in turn, induces strong upward shear forces, causing molten metal to be ejected upward and forming spatter. In contrast, under reduced pressure, the plume density is significantly lower, resulting in minimal attenuation of the laser beam. Consequently, laser energy is transferred to the material in a more stable and continuous manner. This stable energy input leads to more consistent molten pool dynamics, thereby minimizing spatter generation. These observations suggest that pressure reduction contributes to spatter suppression by stabilizing both the laser-material interaction and the behavior of the molten pool.

4. Summary

In this study, the spatter suppression mechanism in keyhole-mode laser welding under reduced ambient pressure was investigated through a combination of X-ray transmission imaging and two-color temperature measurements. The key findings are summarized as follows:

1. Keyhole Morphology and Stability: X-ray imaging revealed that at pressures of 10^3 Pa and above, the keyhole capillary exhibited an unstable wedge-shaped profile, while at 10^2 Pa and below, it transitioned to a more uniform, cylindrical shape. The keyhole capillary depth and area increased significantly with decreasing pressure, reaching maximum values at 10^2 Pa.
2. Molten Pool Dynamics: Temperature distributions obtained using two-color pyrometry indicated that the molten pool area, defined as regions exceeding the melting point of iron (1500 °C), was significantly larger under reduced pressure. At 10^2 Pa, the molten pool area was approximately 1.8 times greater than at atmospheric pressure (10^5 Pa), indicating enhanced energy coupling and thermal stability.
3. Spatter Suppression Mechanism: Under atmospheric pressure, periodic plume formation leads to intermittent laser attenuation, resulting in fluctuating energy input and unstable molten pool contraction, which promotes spatter generation. In contrast, under reduced pressure, plume density is markedly diminished, allowing consistent laser energy delivery. This stabilizes the molten pool and significantly reduces spatter formation.

These findings demonstrate that reduced ambient pressure not only alters the thermal and geometric characteristics of the molten pool and keyhole capillary but also plays a critical role in stabilizing the laser welding process, thereby enabling high-quality, low-spatter welds. The proposed mechanism provides a basis for future optimization of laser welding conditions, particularly in precision applications where spatter must be minimized.

References

[1] K. Ohishi and H. Fujii, “Technical Topics and Automobile Applications of Friction Stir Welding,” Mater. Japan, 53, 603-607 (2014).

[2] T. Miyamichi, “Application of Friction Stir Welding to Railroad Carbody,” DENKI-SEIKO [ELECTRIC Furn.STEEL], 78, 141-147 (2007).

[3] Y. Kawahito et al., “Relationship between melt flows based on three-dimensional X-ray transmission in situ observation and spatter reduction by angle of incidence and defocusing distance in high-power laser welding of stainless steel,” Weld. Int., 32, 485-496 (2018).

[4] S. Katayama Y. Kobayashi, M. Mizutani, and A. Matsunawa, “Effect of vacuum on penetration and defects in laser welding,” J. Laser Applications., 13, 187-192 (2001).

[5] Y. Naito, M. Tokunaga, and T. Sakamoto, “Evaluation of amount of spatter during laser welding under the low-vacuum,” J. JAPAN Weld. Soc., 97, 152-153 (2019).

[6] Y. Arata, N. Abe et al., “Fundamental phenomenon during vacuum laser welding,” J. laser applications, 1984, 1-7 (1984).

[7] Y. Abe, M. Mizutani, Y. Kawahito, and S. Katayama, “Deep penetration welding with high power laser under vacuum,” J. Laser Applications, Proc. 2010, 648-653 (2010).

[8] S. Katayama et al., “Development of Deep Penetration Welding Technology with High Brightness Laser under Vacuum,” Physics Procedia, 12, 75-80 (2011).

[9] Y. Sato et al., “In Site X ray observation of keyhole dynamics for laser beam welding of stainless steel with 16 kW disk laser,” J. Laser Applications, 33, 042-046 (2022).

[10] Meng Jiang, Xi Chen, Yanbin Chen, Wang Tao, “Increasing keyhole stability of fiber laser welding under reduced ambient pressure,” J. Materials Processing Tech, 268, 213-222 (2019).

[11] Peter Berger, Helmut Hugel, Thomas Graf, “Understanding Pore Formation in Laser Beam Welding,” Physics Procedia, 12, 241-247 (2011).

[12] Ishige, Yuta et al., “Blue laser-assisted kW-class CW NIR fiber laser system for high-quality copper welding,” in Proceedings of SPIE, 11668 (2021).

[13] S. Li, G. Chen, M. Zhang, Y. Zhou, Y. Zhang, “Dynamic keyhole profile during high-power deep-penetration laser welding,” J. Materials Processing Tech, 214, 565-570 (2014).

[14] T. Saito et al., “Development of a method for measuring flame temperature distribution in a cylinder using a two-color high-speed shutter TV camera,” Internal Combustion Engine Symposium, Japan, 7, 317-322 (1988).

[15] S. Katayama et al., “Development of Deep Penetration Welding Technology with High Brightness Laser under Vacuum,” Physics Procedia, 12, 75-80 (2011).

[16] Uwe Reisgen et al., “Laser beam welding under vacuum of high grade materials,” Welding in the World, 60, 403-413 (2016).

[17] Y. Habino et al., “On the Viscosity of Liquid Iron,” J. Japan Inst. Met. Mater., 37, 1230-1235 (1973).

[18] A. A. Romanov and V. G. Kochegarov, Lzv. Akad. Nauk SSSR, Met. I Gorn Delo., 1, 41 (1964).

[19] Meng Jiang et al., “Effect of ambient pressure on interaction between laser radiation and plasma plume in fiberlaser welding,” Vacuum, 138, 70-79 (2017).